Mn^{2+}-Induced Structural Flexibility Enhances the Entire Catalytic Cycle and the Cleavage of Mismatches in Prokaryotic Argonaute Proteins

Lirong Zheng,[1,†] Bing Zan,[1,†]Yu Yang,[2,†] Bingxin Zhou,[1,*] Nuolan Li,[2] Banghao Wu,[2] Fan Jiang,[1] Yan Feng,[2] Qian Liu,[2,*] Liang Hong[1,3,4,*]

[1]Institute of Natural Sciences & School of Physics and Astronomy, Shanghai Jiao Tong University, Shanghai 200240, China.

[2]State Key Laboratory for Microbial Metabolism, School of Life Sciences and Biotechnology, Shanghai Jiao Tong University, Shanghai 200240, China.

[3]Shanghai National Center for Applied Mathematics (SJTU center), Shanghai Jiao Tong University, Shanghai 200240, China.

[4]Zhangjiang Institute for Advanced Study, Shanghai Jiao Tong University, Shanghai 200240, China.

[†]These authors contributed equally to this work.

*Corresponding author:

Liang Hong, hongl3liang@sjtu.edu.cn

Qian Liu, liuqian1018@sjtu.edu.cn

Bingxin Zhou, bingxin.zhou@sjtu.edu.cn

Abstract

Prokaryotic Argonaute (pAgo) proteins, a class of DNA/RNA-guided programmable endonucleases, have been extensively utilized in nucleic acid biosensors. The specific binding and cleavage of nucleic acids by pAgo proteins, which are crucial processes for their applications, are dependent on the presence of Mn^{2+} bound in the pockets, as already verified through X-ray crystallography. However, a comprehensive understanding of how dissociated Mn^{2+} in the solvent affects the catalytic cycle, and its underlying regulatory role in this structure-function relationship, remains underdetermined. By combining experimental and computational methods, this study reveals that unbound Mn^{2+} significantly enhances the flexibility of diverse pAgo proteins, regardless of their classification as hyperthermophiles, thermophiles, or mesophiles. This increase in flexibility through decreasing the number of hydrogen bonds, induced by Mn^{2+}, leads to higher affinity for substrates, thus facilitating cleavage. More importantly, Mn^{2+}-induced structural flexibility increases the mismatch tolerance between guide-target pairs by increasing the conformational states, thereby enhancing the cleavage of mismatches. Further simulations indicated that the enhanced flexibility in linkers triggers conformational changes in the PAZ domain for recognizing various lengths of nucleic acids. Additionally, the Mn^{2+}-induced dynamic alterations of the protein cause a conformational shift in the N domain and catalytic sites towards their functional form, resulting in a decreased energy penalty for target release and cleavage. These findings demonstrate that the dynamic conformations of pAgo proteins, resulting from the presence of the unbound Mn^{2+}, significantly promote the catalytic cycle of endonucleases and the tolerance of cleavage to mismatches. This flexibility enhancement mechanism serves as a general strategy employed by Ago proteins from diverse prokaryotes to accomplish their catalytic functions and provide useful information for Ago-based precise molecular diagnostics.

Introduction

Prokaryotic Argonaute (pAgo) proteins, a class of endonucleases that play a crucial role in DNA interference in prokaryotic organisms (1-3), have gained significant attention in the field of biotechnology and medicine for their ability to target and cleave specific sequences in DNA/RNA (4-11). One of the most important applications is diagnostics, where pAgo proteins can be utilized to design molecular diagnostic assays that detect and quantify specific nucleic acid sequences, such as pathogens or cancer-associated mutations (6, 7, 12-14). These assays can lead to the development of more sensitive and specific diagnostic methods, greatly improving the early detection and accurate treatment of diseases. Another crucial use of pAgo proteins is to label nucleic acids both *in vitro* and *in vivo* (15-18). Their high affinity to the substrate, stability in complex, and specific recognition of the target sequence offer significant advantages over traditional methods that rely on nucleic acid binding, such as DNA-painting and DNA fluorescence in situ hybridization (FISH) technology. Furthermore, the combined action of pAgo proteins and nuclease-deficient RecBC helicase can cleave double-strand DNA (10), potentially leading to the design of gene therapies that specifically target disease-causing genes. These applications of pAgo proteins provide new possibilities for the development of therapeutics and genetic manipulation technologies.

pAgo proteins predominantly contain six domains, including the N-terminal domain, Linker1, PIWI-Argonaute-Zwille domain (PAZ), Linker2, middle domain (MID), and P-element Induced Wimpy Testis domain (PIWI) (3, 19, 20). Importantly, the structural dynamics of these domains are critical for the biofunction of pAgo proteins (21-26). The pAgo proteins bind to guide nucleic acids, with the 5'-end and 3'-end of the nucleic acid being accommodated in the basic pocket of the MID domain and the PAZ domain, respectively (27). This guide-loaded complex then searches for complementary target strands through base-pairing with the seed region of the guide strand, which is followed by the propagation of the nucleic acid duplex (21, 27). Subsequently, the 3'-end of the guide is released from the PAZ domain, and the active site of the Glu-finger is closed for correct base-pairing (21). Conformational changes of the catalytic tetrad in the PIWI domain then allow for the cleavage of the target strand (21). Finally, the N domain helps

88 to release the cleaved target, and the protein-guide complex is rearranged to its initial
89 conformation for the next round of cleavage (28, 29).

90 In particular, the presence of Mn^{2+} is crucial for the catalytic activity of pAgo proteins,
91 as determined by their crystal structures (21, 25, 30-34). Most known pAgo proteins
92 utilize one Mn^{2+} bound to the MID pocket for interactions with the 5'phosphate in the
93 guide strand, and two Mn^{2+} ions bound to the catalytic sites (a DEDX motif, where X
94 is K, D, or H) in the PIWI domain for cleavage of the target strand between the 10th and
95 11th bases, counted from the 5'-end of the guide (21, 31). Despite the direct role of these
96 bound Mn^{2+}, a large number of Mn^{2+} are dissociated and present in the solvent.
97 However, the role of these dissociated ions in the catalytic function of pAgo proteins
98 remains unknown. This situation prompts the question of whether these unbound Mn^{2+}
99 in the solvent affect the functional flexibility of pAgo proteins and, subsequently,
100 influence the endonuclease activity of pAgo proteins.

101 In this study, we employed a combination of differential scanning fluorimetry (DSF),
102 nano differential scanning calorimetry (nanoDSC), circular dichroism (CD) spectrum
103 synchrotron small-angle X-ray scattering (SAXS), biochemical assays, and molecular
104 dynamics (MD) simulation to investigate the impact of unbound Mn^{2+} on the structural
105 dynamics and endonuclease activity of prokaryotic Argonaute (pAgo) proteins from
106 mesophilic (*Clostridium butyricum* Ago (*Cb*Ago) (31), *Paenibacilllus borealis* Ago
107 (*Pb*Ago) (35), *Pseudooceanicola lipolyticus* Ago (*Pli*Ago) (30), and *Brevibacillus*
108 *laterosporus* Ago (*Bl*Ago) (35)), thermophilic (*Thermus thermophilus* Ago (TtAgo))
109 and hyperthermophilic (*Pyrococcus furiosus* Ago (*Pf*Ago) (36), *Methanocaldococcus*
110 *fervens* Ago (*Mf*Ago) (37) and *Ferroglobus placidus* Ago (*Fp*Ago) (38)) organisms.
111 Our results indicate that the presence of unbound Mn^{2+} will significantly reduce the
112 hydrogen bonds in pAgo proteins from mesophiles to hyperthermophiles. This
113 reduction in hydrogen bonds grants the protein a large degree of structural flexibility,
114 while the overall packing of the protein remains intact. Furthermore, we demonstrated
115 that Mn^{2+}-dependent dynamics of pAgo proteins show a higher affinity to substrates
116 and thus greatly promote the binding between the guide and target strands, which is key
117 to facilitating the cleavage activity. Remarkably, Mn^{2+} exerts a significant influence on

118 the precision of target DNA cleavage by the protein-target complex, which increases
119 mismatch tolerance between guide-target pairs by increasing the conformational states.
120 All-atom MD simulations at the conditions mimicking the Mn^{2+}-present solvent
121 environment revealed that the flexibility of Link1 and Link2 is greatly enhanced after
122 incubating with Mn^{2+}, which induces the conformational change of the PAZ domain to
123 recognize various lengths of guide strands. Additionally, the increased flexibility in the
124 Glue-finger and the PAZ domain could help the propagation of duplexes. Furthermore,
125 the Mn^{2+}-induced dynamical change shifts the conformation of catalytic sites and the
126 N domain towards its functional form, lowering the energy penalty for target strand
127 cleavage and release, respectively. Overall, our data revealed that the unbound Mn^{2+}-
128 induced flexibility of pAgo proteins is crucial for their catalytic functions, and these
129 findings are generally valid for pAgo proteins obtained from various prokaryotes.
130 Moreover, this study sheds light on the underlying molecular mechanisms of the
131 catalytic cycle of pAgo proteins, providing new avenues for research in the field of
132 prokaryotic immunity systems and precise molecular diagnostics.
133

134 **Results**

135 **Mn^{2+} enhances the flexibility of pAgo proteins obtained from mesophiles,**
136 **thermophiles, and hyperthermophiles**

137 The molecular architecture of long pAgo proteins is characterized by a distinct two-
138 lobed structure, which is a common feature among members of this family (3, 22) (as
139 shown in Figure 1A). The first lobe comprises the N domain, Linker1, and PAZ domain,
140 while the second lobe comprises the Linker2, MID domain, and PIWI domain (as
141 shown in Figure 1B). The phylogenetic position of pAgo proteins studied herein, as
142 well as their structural characteristics, are presented in Figure 1C and Figure S1,
143 respectively. Although the overall packing topology of pAgo proteins obtained from
144 different prokaryotes exhibits a similar tertiary and secondary structure (as shown in
145 Figure S1), their functions and optimal physiological temperatures are vastly divergent
146 (3, 24).

147 We first examined how the secondary structures of pAgo proteins vary with the
148 concentration of Mn^{2+} at their respective physiological temperatures. The study was
149 conducted using CD spectroscopy, a technique that measures the secondary structure of
150 a protein by analyzing its absorption of circularly polarized light (39). The results, as
151 shown in Figure S2, indicate that the presence of Mn^{2+} does not significantly alter the
152 secondary structures of pAgo proteins.

153 We then characterized the effect of Mn^{2+} on the thermostability of pAgo proteins by
154 using DSF spectroscopy. The DSF method is a quantitative method that allows for the
155 assessment of thermostability by measuring changes in fluorescence intensity as the
156 temperature is progressively increased, which monitors the tertiary structural changes
157 in proteins (40). The melting temperature (T_m) of the tertiary structure of different pAgo
158 proteins was determined with and without the presence of Mn^{2+}. As shown in Figures
159 1D-J, the results revealed that the addition of Mn^{2+} resulted in a significant decrease in
160 the T_m of pAgo proteins, reducing the thermostability. To further validate these findings,
161 the melting temperature of pAgo proteins was also determined using nanoDSC, a
162 technique that measures the heat capacity of a protein as a function of temperatures (41).
163 The results obtained through nanoDSC were consistent with those obtained through
164 DSF spectroscopy, showing a similar trend of increased denaturation in the presence of
165 Mn^{2+} (as shown in Figure S3). It is noteworthy that no significant difference was
166 observed when the T_m of the secondary structure of pAgo proteins was evaluated under
167 similar conditions (see Figure S4). Thus, the above results suggest that the presence of
168 Mn^{2+} may disrupt interactions between amino acids participating in the tertiary
169 structure of the protein but not those involved in the secondary structure (alpha-helix
170 and beta-sheet), thereby reducing the thermostability of the protein.

171

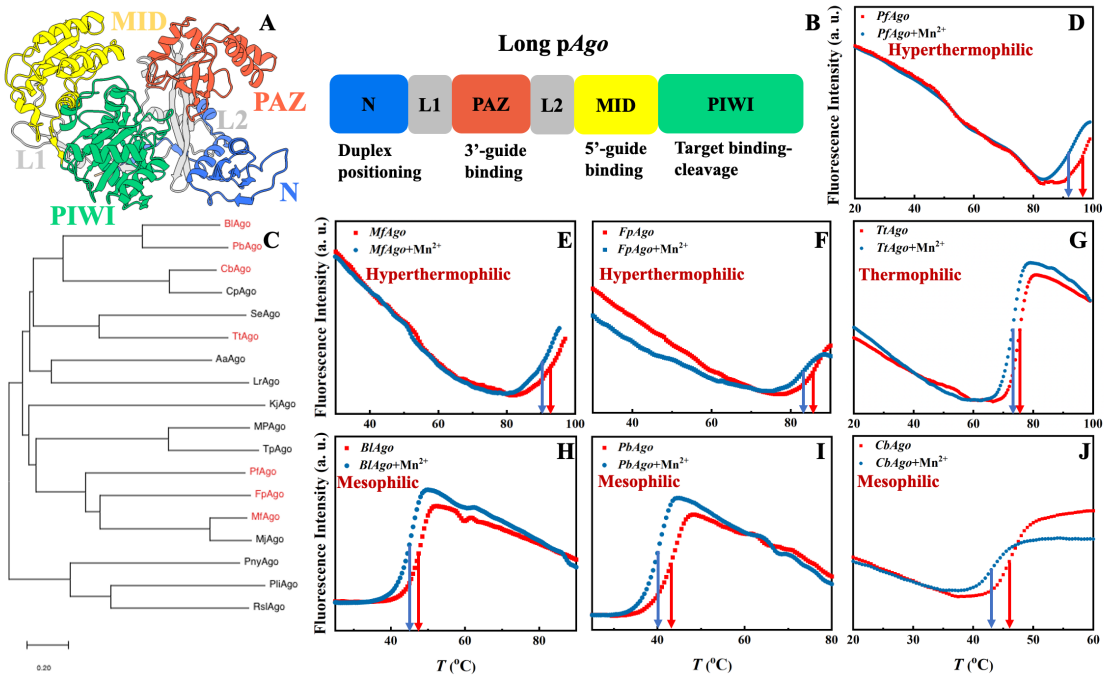

Figure 1. Structural analysis of hyperthermophilic, thermophilic, and mesophilic pAgo proteins incubated with and without Mn^{2+} at different temperatures. (A) Representation of the domain architectures of long pAgo proteins. PAZ domain, MID domain, N domain, and PIWI domain are colored in red, yellow, blue, and green, respectively. (B) Schematic diagram of the domain organization of long pAgo proteins. (C) Maximum likelihood phylogenetic tree of characterized pAgo proteins. DSF spectra of (D) *Pf*Ago, (E) *Mf*Ago, (F) *Fp*Ago, (G) *Tt*Ago, (H) *Bl*Ago, (I) *Pb*Ago, and (J) *Cb*Ago incubated with and without Mn^{2+} measured at different temperatures. The concentration of Mn^{2+} is 5 mM, which is widely applied in the biochemical assay of pAgo proteins. The solid arrows in panels D-J indicate the melting temperature, T_m.

In order to gain a deeper understanding of the structural factors that contribute to the observed difference in T_m between pAgo proteins incubated with Mn^{2+} and those incubated without, we conducted all-atom molecular dynamics (MD) simulations on mesophilic (*Cb*Ago), thermophilic (*Tt*Ago), and hyperthermophilic (*Fp*Ago) pAgo proteins incubated with and without Mn^{2+}. The example of snapshots of MD simulations is shown in Figure S5 (The example of the potential energy of protein as a function of MD simulation time is shown in Figure S6). Our simulations reveal that the pAgo proteins incubated without Mn^{2+} exhibit a greater number of hydrogen bonds when compared to those incubated with Mn^{2+}, while the number of salt bridges remains constant (see Table 1). This disparity in intermolecular interactions, i.e., loss of

hydrogen bonds, could reduce the energy barrier for protein unfolding in pAgo proteins incubated with Mn^{2+}, which explains the decreased T_m observed in pAgo proteins observed in Figures 1D-J.

By integrating the results of CD, DSF, and MD simulations, it suggests that Mn^{2+} possesses the capacity to perturb the intermolecular interactions among amino acid residues participating in the building of the tertiary structure, while not for the secondary structure (see Table S1).

Table 1. Number of hydrogen bonds and salt bridges of pAgo proteins incubated with and without Mn^{2+}

Protein	*Fp*Ago	*Fp*Ago+Mn^{2+}	*Tt*Ago	*Tt*Ago+Mn^{2+}	*Cb*Ago	*Cb*Ago+Mn^{2+}
Hydrogen bond*	611	588	452	438	307	282
Salt bridge*	13	13	11	11	9	9

*Number of hydrogen bonds and salt bridges are averaged over the entire simulation time.

It has been reported that structural flexibility is crucial for the biofunction of pAgo proteins (22, 24). The intriguing question then arises as to whether the decreased intermolecular interactions resulting from the addition of Mn^{2+} can increase the flexibility of pAgo proteins. To address this, we conducted a structural analysis of four different types of pAgo proteins, namely *Fp*Ago (hyperthermophilic), *Tt*Ago (thermophilic), *Bl*Ago (mesophilic), and *Cb*Ago (mesophilic) using synchrotron small-angle X-ray scattering (SAXS) and Porod-Debye analysis (24, 42, 43). The Porod-Debye analysis, which is a combination of the scattering intensity and the fourth power law of the scattering wavevector, $q^4 \cdot I(q)$, can be utilized to reveal the flexibility of biomacromolecules (42). An unambiguous Porod plateau in the scattering profile indicates the protein takes a rigid structure, while a lack of a plateau implies that the biomacromolecule forms dynamic conformations (42). As shown in Figures 2A-D, the Porod-Debye plots of *Fp*Ago, *Tt*Ago, *Bl*Ago, and *Cb*Ago all displayed a clear Porod plateau. However, after incubation with Mn^{2+}, a significant change in the Porod-Debye region was observed, with a loss of the plateau suggesting the protein flexibility is

223 greatly increased in the presence of Mn^{2+} (see Figures 2A-D). To further support these
224 findings, we compared the flexibility of pAgo proteins incubated with and without Mn^{2+}
225 using root mean square fluctuation (RMSF) derived from MD simulations. The RMSF
226 of pAgo proteins incubated with Mn^{2+} is found to be larger than pAgo proteins
227 incubated without Mn^{2+}, indicating that Mn^{2+} confers increased flexibility to pAgo
228 proteins (Figures 2E-H). Our findings demonstrate that Mn^{2+} has a universal effect to
229 enhance the structural dynamics of pAgo proteins from different prokaryotes.

230 Furthermore, we also compared the structural compactness of pAgo proteins
231 incubated with and without Mn^{2+}. By utilizing Guinier analysis (44, 45), one can derive
232 the radius of gyration (R_g) of the protein molecule, and we found that R_g of pAgo
233 proteins incubated with Mn^{2+} is comparable to that of pAgo proteins incubated without
234 Mn^{2+} (Figures 2I, S7-S17, and Table S3), which is in agreement with the R_g derived
235 from MD simulations (Figure S18). Furthermore, the Porod volume of pAgo proteins
236 incubated with and without Mn^{2+} was found to be similar, indicating that Mn^{2+} does not
237 have a significant impact on the overall compactness of pAgo proteins. These findings
238 were also supported by the *ab initio* low-resolution model reconstructed from SAXS
239 data. As shown in Figure S19, the *ab initio* structure of pAgo proteins incubated with
240 Mn^{2+} is found to be similar to that of pAgo proteins incubated without Mn^{2+}.

241 The findings from DSF, CD, nanoDSC, SAXS, and MD simulation studies provide
242 a convincing explanation of Mn^{2+}'s impact on the structural flexibility of pAgo proteins,
243 which suggests that the presence of Mn^{2+} greatly enhances the protein flexibility while
244 preserving the protein's secondary structure. The observation that the overall structure
245 of pAgo proteins remains similar to the crystalline form when incubated with Mn^{2+}
246 further supports this conclusion, indicating that the flexibility changes are not due to
247 significant alterations in the protein's overall structure.

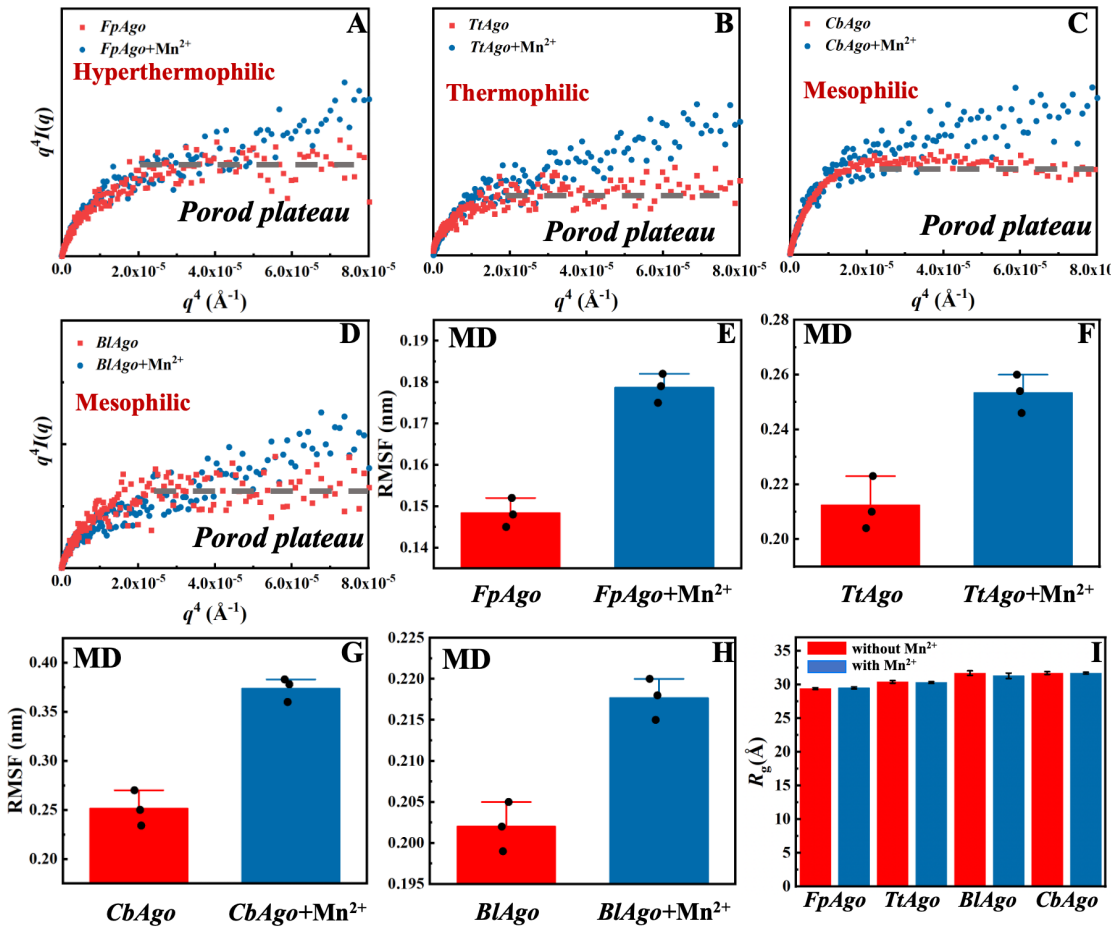

Figure 2. Structures and dynamics of pAgo proteins incubated with and without Mn^{2+} derived from SAXS and MD simulation. Porod-Debye analysis, $q^4I(q)$ vs. q^4, of (A) *Fp*Ago, (B) *Tt*Ago, (C) *Bl*Ago, and (D) *Cb*Ago incubated with and without Mn^{2+}. The concentration of Mn^{2+} is 5 mM. The dashed gray line in each panel indicates the Porod plateau. The details about the SAXS data collection and analysis are summarized in Materials and Methods. Comparison of root mean squared fluctuation (RMSF) of (E) *Fp*Ago, (F) *Tt*Ago, (G) *Cb*Ago, and (H) *Bl*Ago incubated with and without Mn^{2+}. RMSF of pAgo proteins is averaged over entire residues. The results from three independent MD simulations were quantified. Error bars represent the standard deviations of three independent simulations. The detailed procedure is presented in the Materials and Methods. (I) The radius of gyration (R_g) of *Fp*Ago, *Tt*Ago, *Bl*Ago, and *Cb*Ago incubated with and without Mn^{2+} derived from SAXS. The Guinier plots of proteins are shown in Figures S7-S17.

Enzymatic functional role of the Mn^{2+} induced flexibility in pAgo proteins

The physical characterization of Mn^{2+} has revealed that it can enhance the flexibility of pAgo proteins. However, the implications of this increase in flexibility on the catalytic function of pAgo proteins remain unclear. As shown in Figure 3A, the catalytic cycle of pAgo proteins involves several functional steps, including binding guide (gDNA

268 binding), target recognition and annealing (tDNA binding), target cleavage, and release
269 (tDNA cleaving and releasing) (22, 46). In order to study the impact of increased protein
270 structural flexibility on guide DNA binding, we employed the fluorescence polarization
271 assay on *Pli*Ago (DSF measurements of *Pli*Ago incubated with and without Mn^{2+} are
272 shown in Figure S20A), a unique protein that does not require Mn^{2+} for substrate
273 binding as verified by both in vitro assay and crystal resolution (30). The results, as
274 shown in Figure 3B, indicate that as the concentration of Mn^{2+} increases, the dissociate
275 constant K_d decreases, thus demonstrating an increased binding of gDNA to the protein
276 and the formation of the more protein-gDNA binary complex. To further verify these
277 results, we conducted gDNA binding experiments on *Cb*Ago using a mutation on the
278 binding site amino acids, resulting in a binding pocket in the MID domain that does not
279 bind Mn^{2+} (the amino acids sequence is shown in Table S5) (30). We found that the
280 *Cb*Ago mutant (*Cb*Ago*M*) incubated with Mn^{2+} had a greater binding affinity to gDNA
281 than it incubated without Mn^{2+} (as shown in Figure 3C), providing additional support
282 for the notion that the increase in protein flexibility caused by Mn^{2+} can enhance the
283 binding ability of proteins to gDNA (DSF measurements of *Cb*Ago*M* incubated with
284 and without Mn^{2+} are shown in Figure S20B). Additionally, an increased quantity of
285 protein-gDNA binary complexes can effectively function as templates, thereby
286 facilitating the binding of a greater amount of tDNA.

287 The process of cleavage and release of tDNA is of paramount importance for the
288 subsequent rounds of tDNA cleavage mediated by pAgo proteins (22). In order to
289 investigate the impact of Mn^{2+} on the cleavage efficiency of pAgo proteins on tDNA,
290 we employed a highly sensitive fluorescence-based assay. To this end, we labeled the
291 5'- and 3'-end of tDNA with the fluorescent group 6'FAM and quenching group BHQ1,
292 respectively. This allowed us to monitor the cleavage and release process of pAgo
293 proteins on tDNA in real-time, with the absence of a fluorescent signal indicating that
294 tDNA was either not cleaved or had been cleaved but not yet released, and the presence
295 of a fluorescent signal indicating that tDNA had been cleaved and released successfully.
296 As depicted in Figures 3D and E, the cleavage rate and yield of cleavage products of
297 *Pli*Ago and *Cb*Ago*M* on tDNA exhibited a clear dependence on the concentration of

298 Mn^{2+}, with tested higher concentrations resulting in increased cleavage products. Our
299 findings provide important insights into the role of Mn^{2+} in modulating the catalytic
300 activity of pAgo proteins, indicating that the enhancement of protein flexibility brought
301 about by Mn^{2+} might facilitate conformational changes during the cleavage process and
302 the release of products.
303

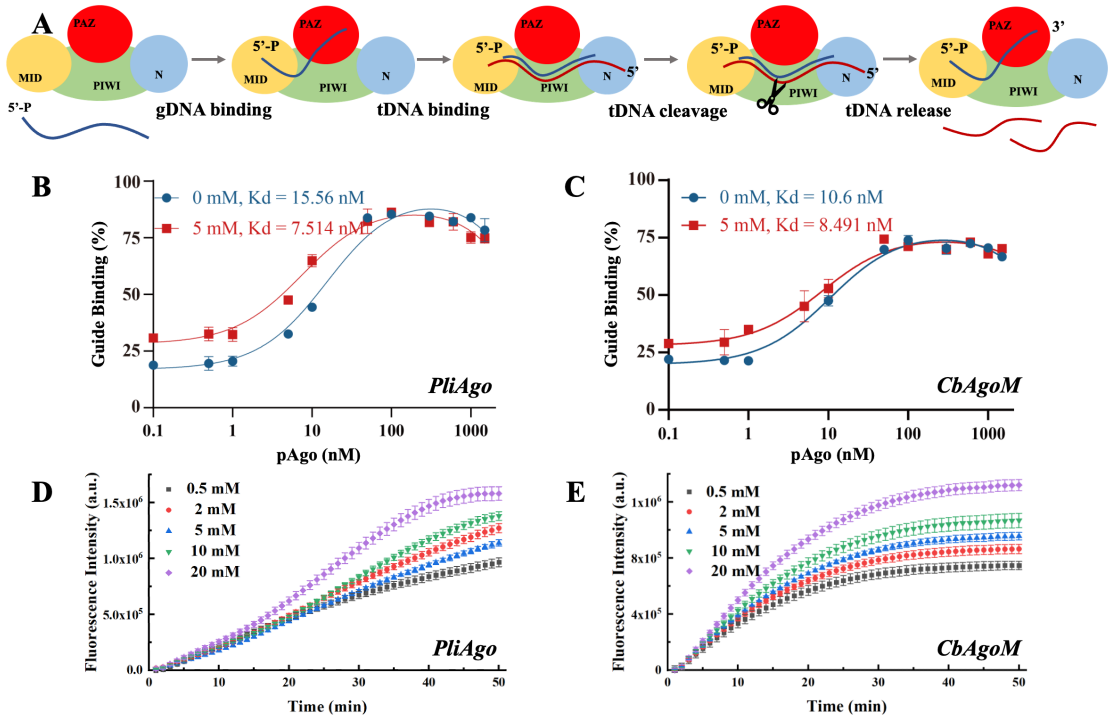

304

305 **Figure 3. The role of the Mn^{2+}-dependent structural dynamics of pAgo proteins**
306 **for binding guide DNA and cleavage of target DNA.** (A) Schematic diagram of
307 DNA-catalytic cycle of pAgo proteins. Fluorescence polarization assay of the binding
308 of (B) *Pli*Ago and (C) *Cb*Ago*M* to gDNA at different concentrations of Mn^{2+}. Cleavage
309 assays of (D) *Pli*Ago and (E) *Cb*Ago*M* incubated with different concentrations of Mn^{2+}.
310 The cleavage activity of pAgo proteins is traced by fluorescence intensity as a function
311 of time. In all experiments, protein, guide, and target were mixed at a 5:1:1 molar ratio
312 and incubated at 37 °C. The reaction buffer without Mn^{2+} contains 10 mM EDTA. Three
313 samples were used for each experimental condition. The results from three independent
314 experiments were quantified. Error bars represent the standard deviations of three
315 independent experiments. The detailed procedure is presented in the Materials and
316 Methods. The nucleotide sequences of the gDNA and tDNA are presented in Table S4.
317

318 It has been reported that small interfering DNA of varying lengths present inside cells
319 can function as gDNA for proteins, which subsequently cleave invading DNA (47). In
320 light of this, we explored the flexibility of pAgo proteins and their potential roles in

321 facilitating binding to tDNA and gDNA of different lengths. Our analysis, illustrated in
322 Figure S21, revealed that when the concentration of Mn^{2+} increases from 0.1 mM to 5
323 mM, K_d for the protein with tDNA and gDNA of various lengths decrease, indicating
324 enhanced binding of gDNA and tDNA to the pAgo protein. These findings suggest that
325 the ability of pAgo proteins to adapt their conformation, facilitated by an increase in
326 structural flexibility induced by Mn^{2+}, enables them to bind to tDNA and gDNA of
327 varying lengths.

328 We then investigated the effect of Mn^{2+}-induced flexibility in proteins on the
329 cleavage and release of tDNA of varying lengths. Our experiments utilized a range of
330 Mn^{2+} concentrations to measure the rate of tDNA cleavage and release. As shown in
331 Figure S22, the results revealed a statistically significant positive correlation between
332 increasing concentrations of Mn^{2+} and the fluorescence intensity per unit of time. This
333 observation demonstrates an augmentation in the rate of tDNA cleavage and release in
334 response to Mn^{2+}-induced changes in pAgo protein flexibility, thus suggesting that the
335 enhancement of pAgo protein flexibility serves as a facilitative mechanism for the
336 cleavage and release of tDNA.

337

338 **Mn^{2+}-dependent precision cleavage of target DNA**

339 It's widely recognized that the efficiency of pAgo's cleavage is influenced by
340 mismatches that occur between the guide and the target, particularly within the seed
341 region. The presence of these mismatches can cause "bubbles" to form between the
342 guide and the target, consequently affecting their mutual recognition and the subsequent
343 cleavage by pAgo (Figure 4A). In the case of *Pf*Ago, the introduction of a single
344 nucleotide mismatch at varying positions within the guide can cause weakening or even
345 elimination of target cleavage (Figure 4B). Interestingly, when the concentration of
346 Mn^{2+} is increased, *Pf*Ago can cleave the target even with a mismatched guide (Figure
347 4B). This suggests that Mn^{2+} enhances the flexibility of *Pf*Ago, thereby increasing its
348 tolerance for mismatches. We then selected three guides that either perfectly matched
349 the target sequence (guide-m0) or contained mismatches at the fourth (guide-m4) and
350 seventh (guide-m7) positions. We performed cleavage assays at gradually increasing

351 Mn^{2+} concentrations (Figures 4C and D). Under conditions of 0.1 mM Mn^{2+}, the three
352 guides directed varied catalytic efficiency, ranging from 20% to 70%. Conversely, when
353 the Mn^{2+} concentration was increased to 1 mM, the cleavage efficiency of all three
354 guides reached a comparable level. Similarly, *Cb*Ago demonstrated enhanced activity
355 with increasing Mn^{2+} concentrations, as shown in Figure S23.

356 In order to further investigate the role of Mn^{2+}, we conducted fluorescence
357 polarization experiments to measure the apparent dissociation constants (K_d) of *Pf*Ago
358 with either the guide or the target at different Mn^{2+} concentrations. We observed that an
359 increase in the concentration of Mn^{2+} enhances the affinity of *Pf*Ago for both the guide
360 and the target. For the guides, the K_d values increased up to 4-fold and 2-fold for guide-
361 m0 and guide-m4, respectively. For the target, the K_d values increased 3-fold (Figure
362 4E). These findings suggest an increased binding affinity of the protein for mismatched
363 gDNA and tDNA, which attributes to increased protein flexibility under elevated Mn^{2+}
364 concentrations. This provides further support for our hypothesis that Mn^{2+} may play a
365 crucial role in enhancing the tolerance of DNA cleavage to mismatches.

366 Thus, the data obtained indicate that the enhancement of flexibility in pAgo proteins,
367 induced by Mn^{2+}, broadens the tolerance for mismatches between the gDNA and the
368 tDNA. This heightened tolerance, however, incurs a trade-off, leading to a consequent
369 decrease in the precision of tDNA cleavage orchestrated by the protein. This pivotal
370 finding underscores the profound implications of the interplay between protein
371 flexibility and nucleic acid detection accuracy, highlighting the necessity for
372 maintaining an optimal balance between these two critical factors.

373

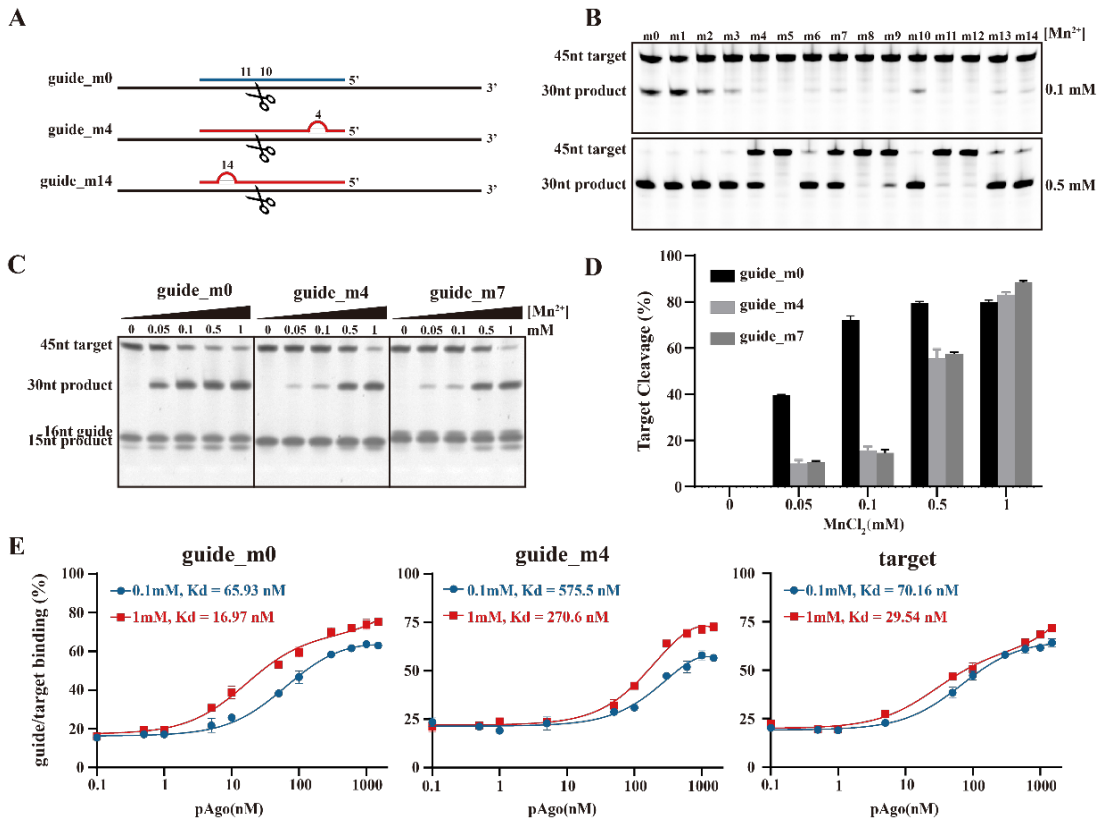

Figure 4. The role of the Mn^{2+}-dependent structural dynamics of pAgo proteins for the designed mismatched guide DNA directed cleavage on target DNA. (A) Schematic representation of the designed mismatched gDNA directed cleavage on tDNA. The introduced mismatched nucleotides are indicated by the red semicircle. The nucleic acids sequence of gDNA and tDNA are shown in Table S6. *Pf*Ago is used here. (B) and (C) Gel detection results for the designed mismatched gDNA-directed cleavage on tDNA at different concentrations of Mn^{2+}. (D) Quantifying the effects of incubating with Mn^{2+} on tDNA cleavage obtained from panel (C). (E) Fluorescence polarization assay of the designed mismatched guide and target at different concentrations of Mn^{2+}. The results from three independent experiments were quantified. Error bars represent the standard deviations of three independent experiments.

Mn^{2+}-dependent dynamical states in pAgo protein derived from MD simulations

To gain a more comprehensive understanding of the effects of Mn^{2+} on the conformational dynamics related to the function of pAgo proteins at the atomic scale, we conducted a detailed examination using MD simulations. This allowed us to analyze structural changes and flexibility in response to the presence of Mn^{2+}. Figure 5A compares the structure of *Cb*Ago incubated with Mn^{2+} (represented in blue) to that of *Cb*Ago without Mn^{2+} (represented in red) over trajectory time. The results show that Mn^{2+} leads to a significant increase in the conformational dynamics of *Cb*Ago

395 compared to it incubated without Mn^{2+}, indicating that Mn^{2+} notably enhances the
396 flexibility of the proteins (as shown in Figure 5B). However, the content of the alpha
397 helix, beta sheet, and turns and loops as terms of secondary structure, as well as the
398 radius of gyration, remain consistent regardless of the presence of Mn^{2+}, in line with
399 the SAXS and CD results presented in Figures 1 and 2. Additionally, when comparing
400 the conformational phase space of *Cb*Ago sampled in the MD simulation with and
401 without Mn^{2+}, we found that the presence of Mn^{2+} allows the protein to explore a
402 significantly larger conformational space (as depicted in Figures 5C and D). This larger
403 conformational space suggests that the presence of Mn^{2+} may lower the energy barrier
404 between different states, thus facilitating the transition between functional states.

405 *Guide binding* The conformational mobility of the PAZ domain, upon incubation
406 with Mn^{2+}, is observed to be significantly greater than that of protein incubated without
407 Mn^{2+} over the course of the trajectory time (see Figures 5E and F). This phenomenon
408 can be attributed to the increased flexibility present in the Linker1 and Linker2 regions
409 between the N domain and the MID domain, respectively (as shown in Figure 5G). The
410 augmented conformational mobility of the PAZ domain, as indicated by the arrows in
411 Figure 5H, could facilitate the capability of various pAgo proteins to engage with
412 diverse populations of short DNAs of varying lengths (21, 22, 25).

413 *Propagation of duplexes and cleavage of target* Figure 5I illustrates the RMSF of the
414 glutamic loop, which houses the catalytic glutamate residue. Our analysis reveals that
415 the glutamic loop experiences a significant increase in flexibility. The binding of the
416 complementary strand target leads to structural modifications of pAgo proteins,
417 including rotations of the PAZ domain and alterations in the conformations of various
418 loops within the PIWI domain (22, 27, 34, 48). These changes propagate the nucleic
419 acid duplex within the catalytic cleft of the pAgo protein and activate catalysis.
420 Specifically, the glutamic loop, as shown in Figure 5I, is able to adopt distinct
421 conformations in the presence of the target strand. It subsequently inserts into the
422 catalytic sites and binds catalytic metal ions during the formation of the extended guide-
423 target duplex. Therefore, the augmented conformational dynamics in the PAZ domain
424 and catalytic loop promote the closure of the binding cleft and activate the cleavage of

425 the target (21, 23). Furthermore, we also observed that the catalytic tetrads adjust their
426 alignments to functional ones, thereby reducing the energy barrier for conformational
427 change (see Figure 5J). In this context, the functional conformation of the catalytic
428 region refers to that in the crystalline structure of the *Cb*Ago-guide-target complex
429 (PDB ID: 4N47).

430 *Target release and preparation for next round catalysis* As shown in Figure 5K, Mn^{2+}
431 induces the position of the N domain to be adjusted closer to its functional conformation,
432 which contributes to promoting the unwinding of the duplex of the guide and target
433 after cleavage (28, 29). Additionally, the increased flexibility in the glutamic loop and
434 Linkers could facilitate the unplugging of the active sites and the restoration of the PAZ
435 domain, respectively, then regenerating the binary guide-pAgo complex for the next
436 round of catalysis. Furthermore, we conducted an analysis of the binding energy (49)
437 of protein to DNA in both the presence and absence of Mn^{2+}. Our results indicate that
438 the binding energy of the protein to DNA is reduced upon the addition of Mn^{2+} ions
439 throughout the simulation time. This finding also suggests that the presence of Mn^{2+}
440 can facilitate the release of cleaved tDNA and promote the re-adjustment of
441 conformations (see Figures 5L and 5M).

442

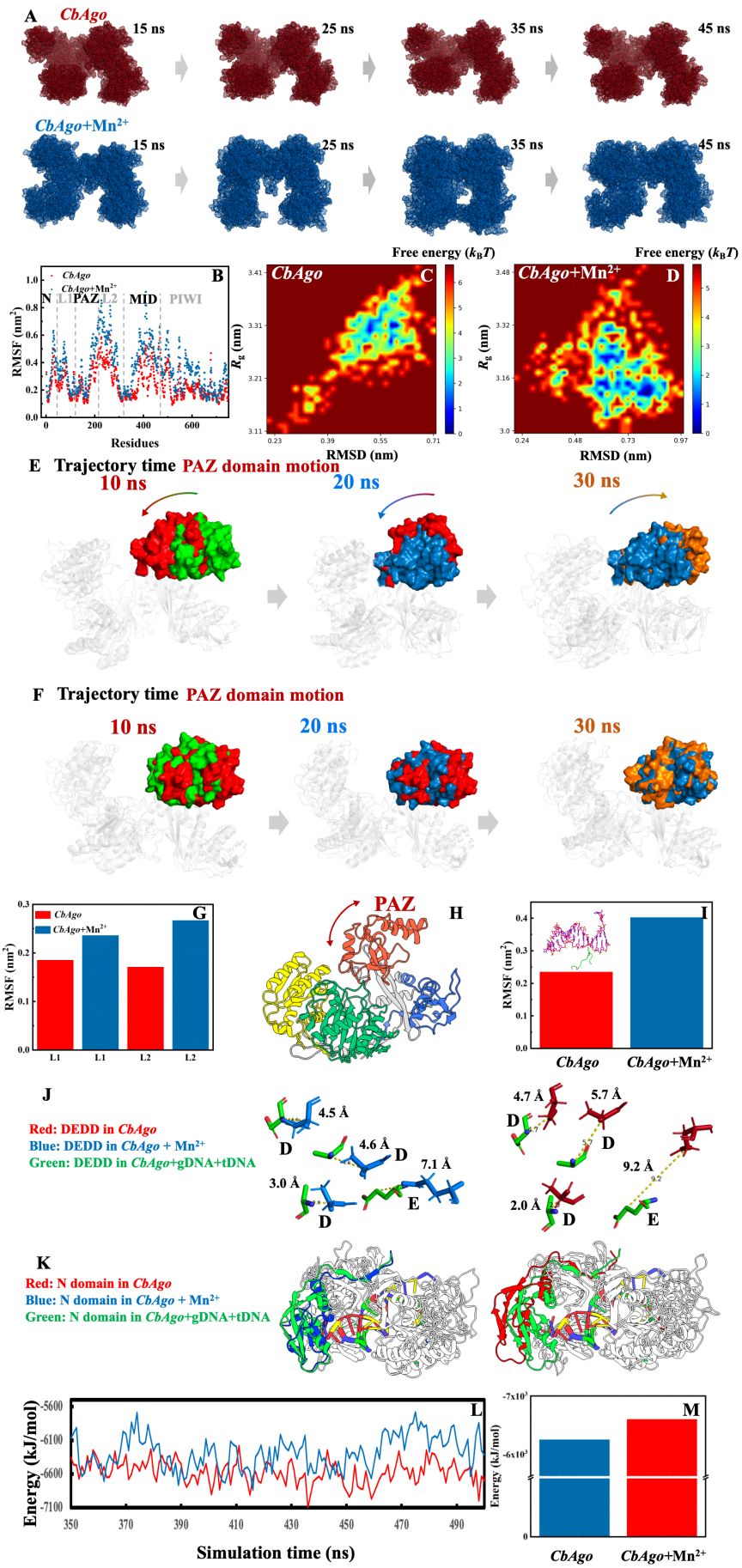
A
CbAgo
15 ns
25 ns
35 ns
45 ns
CbAgo+Mn2+
B
RMSF (nm2)
Residues
N
L1
PAZ
L2
MID
PIWI
C
D
Free energy (kBT)
Rg (nm)
RMSD (nm)
E Trajectory time PAZ domain motion
10 ns
20 ns
30 ns
F Trajectory time PAZ domain motion
G
H
PAZ
I
J
Red: DEDD in CbAgo
Blue: DEDD in CbAgo + Mn2+
Green: DEDD in CbAgo+gDNA+tDNA
4.5 Å
4.6 Å
7.1 Å
3.0 Å
4.7 Å
5.7 Å
9.2 Å
2.0 Å
K
Red: N domain in CbAgo
Blue: N domain in CbAgo + Mn2+
Green: N domain in CbAgo+gDNA+tDNA
L
Energy (kJ/mol)
Simulation time (ns)
M

Figure 5. The effect of Mn^{2+} on the structural dynamics of pAgo protein derived from MD simulations. (A) The MD-derived structure of *Cb*Ago incubated with (blue) and without (red) the presence of Mn^{2+} at different simulation times. (B) Comparison of RMSF of the overall structure. Free energy landscape of *Cb*Ago incubated (C) without and (D) with Mn^{2+}. RMSD is the root mean squared deviation of the structure in the first MD snapshot after equilibration. Conformational change of PAZ domain in *Cb*Ago incubated (E) with and (F) without Mn^{2+} obtained from MD simulation. Comparison of RMSF of (G) linkers and (I) catalytic loop of *Cb*Ago incubated with and without Mn^{2+}. (H) Scheme of the motion of PAZ domain in pAgo protein. (J) Structural alignment of catalytic sites of *Cb*Ago incubated without (left panel) and with (right panel) Mn^{2+} with respect to that of the experimental functional conformation (PDB ID: 6qzk). Catalytic sites, DEDD, in *Cb*Ago incubated without Mn^{2+}, with Mn^{2+}, and in the experimental functional form are highlighted in red, blue, and green, respectively. (K) Structural alignment of N domain of *Cb*Ago incubated without (left panel) and with (right panel) Mn^{2+} with respect to that of the experimental functional conformation (PDB ID: 6QZK). N domain in *Cb*Ago incubated without Mn^{2+}, with Mn^{2+}, and in the experimental functional form is highlighted in red, blue, and green, respectively. Here, the protein structure is aligned by PyMOL. The alignment on C_{alpha} is achieved by using PyMOL software. (L) The binding energy of *Cb*Ago to gDNA/tDNA duplex over the entire simulation time derived from MD simulations. (M) The averaged binding energy of *Cb*Ago to gDNA/tDNA duplex. The initial structure of MD simulation is the protein-gDNA-tDNA tertiary complex (PDB ID: 6QZK).

Discussion

Divalent cations play a fundamental role in biomacromolecule dynamics, primarily situated in ribosomes (50, 51), enzymes (30, 52, 53), and structural proteins (54). The proper function and stability of such proteins necessitate the presence of ions. Divalent ions can impart consequential effects on the conformation and functionality of proteins, which is integral to numerous biological processes like enzymatic catalysis (31), regulation of protein-protein interactions (54), and signal transduction (55). Divalent ions also play a pivotal role in the regulation of membrane transport phenomena like ion transit across the plasma membrane and intracellular movement of ions and molecules (56). In ion channels and pumps, divalent ions serve as indispensable regulators, controlling the opening and closing of these channels, thereby regulating the flux of ions into and out of cells (56). Additionally, it has been demonstrated that ions impact the activity of endonucleases. For instance, the Mg^{2+}-dependent conformational

480 rearrangements of the CRISPR-Cas12a R-loop complex are crucial for complete
481 double-stranded DNA cleavage (52).

482 In the case of pAgo proteins, we unraveled the molecular mechanisms of unbound
483 Mn^{2+} regulating the binding, cleavage, and release of products through the use of
484 spectroscopy, biochemical assays, and MD simulation. Initially, the presence of Mn^{2+}
485 can disrupt certain hydrogen bonds within non-secondary structures, thereby increasing
486 the flexibility of proteins and the associated entropy, without compromising the
487 structural integrity. Next owing to the increased flexibility of the L1 linker and L2 linker,
488 the conformational number of the PAZ domain is significantly increased. This enhanced
489 structural flexibility facilitates the binding of the pAgo protein to gDNA, and helps the
490 PAZ domain recognize gDNA of varying lengths. Furthermore, the enhanced structural
491 variability of the glutamic loop and PAZ domain aids in the propagation of the DNA
492 duplex, preparing it for tDNA cleavage. In addition, once the holo-form arrangement is
493 achieved by the catalytic sites and the N domain, the catalytic center in the PIWI domain
494 can be exposed to the tDNA. This exposure allows for the cleavage of the tDNA,
495 facilitating the release of the cleaved product. Our simulation data indicates that the
496 energy barrier for releasing the target in this step is also lowered by the presence of
497 Mn^{2+}. The analysis of the conformational dynamics of this catalytic cycle reveals that
498 the presence of Mn^{2+} reduces the energy barrier for conformational changes between
499 different functional conformations. Furthermore, this result unveiled the unexpected
500 dynamical role of unbound Mn^{2+} in increasing the conformation states of pAgo proteins,
501 which is crucial for their catalytic functions.

502 Previous structural research, based on crystallography, has demonstrated that pAgo
503 proteins must undergo significant conformational changes to implement their functions,
504 including the rearrangement of catalytic tetrads, propagation of duplexes through
505 shifting loops in the PIWI domain, and motion of the PAZ domain, and release of
506 cleaved targets by adjusting the PAZ and N domains (21). Therefore, structural
507 flexibility is crucial for the conformational arrangement needed to achieve the
508 functionality of pAgo proteins at different stages. In our study, we found that pAgo

509 proteins from mesophiles, thermophiles, and hyperthermophiles exhibit a significant
510 increase in flexibility when unbounded Mn^{2+} is present.

511 Moreover, it has been demonstrated that pAgo proteins widely participate in hosts to
512 defend against the invasion of nucleic acids (2). Living organisms contain DNA or RNA
513 of different lengths and sequences, and invading nucleic acids also vary in their lengths
514 and sequences (47). We hypothesize that pAgo proteins might need to modify their
515 conformations to bind with different types of DNA or RNA in order to identify the
516 invading nucleic acid. In this scenario, the flexibility of pAgo proteins, induced by Mn^{2+},
517 may play a crucial role as it allows the protein to efficiently recognize the invader and
518 protect the host.

519 The precision of nucleic acid detection methodologies is critically reliant on the
520 accurate cleavage by pAgos. The high fidelity of such assays is underpinned by the
521 exactness of the initial DNA cleavage process. Any deviations or inaccuracies within
522 this fundamental step can substantially diminish the efficiency of subsequent
523 amplification and signal readout stages (6). Our findings shed light on the role of Mn^{2+}-
524 induced flexibility in augmenting the proficiency of the pAgo protein in handling
525 mismatches between gDNA and tDNA. We observed a correlation between increased
526 concentrations of Mn^{2+} and an enhanced capacity of the pAgo protein to accommodate
527 gDNA and tDNA mismatches, facilitating tDNA cleavage. The elevated presence of
528 Mn^{2+} could enhance the protein's conformational flexibility and various functional
529 states, which is verified by the MD simulations. This increased structural flexibility
530 enables the protein to adapt its conformational state to cater to a variety of mismatch
531 scenarios, thus improving the efficiency of tDNA cleavage. These findings carry
532 significant implications for the effectiveness of various recently developed nucleic acid
533 detection technologies (5, 6).

534

535 **Conclusion**

536 In the present study, we investigated how the unbound Mn^{2+}-affect the dynamics,
537 structure, and endonuclease activity of prokaryotic pAgo proteins obtained from
538 mesophilic (*Cb*Ago, *Bl*Ago, *Pli*Ago, and *Pb*Ago), thermophilic (*Tt*Ago), and

539 hyperthermophilic (*Pf*Ago, *Fp*Ago, and *Mf*Ago) organisms using a combination of
540 experimental and computational methods. Our results indicate that the presence of these
541 unbound free Mn^{2+} significantly reduces the hydrogen bonds in different pAgo proteins
542 to release a great degree of structural flexibility while maintaining the overall structural
543 integrity. Biochemical assays revealed that this Mn^{2+}-induced structural flexibility in
544 pAgo proteins significantly increases the substrate affinity and facilitates the binding
545 of guide and target strands compared to the proteins without Mn^{2+}. Complementary
546 computer simulations confirmed these experimental findings and revealed that the
547 increased flexibility of Linker1 and Linker2 promotes the conformational mobility of
548 the PAZ domain, allowing for the recognition of guide and target strands of varying
549 lengths. Additionally, changes in the conformations of the PAZ domain and glutamic
550 finger promote the propagation of the duplex. By comparing the structures of pAgo
551 proteins incubated with Mn^{2+} to those of the protein-guide-target ternary complex, we
552 observed that the conformation of catalytic sites and N domain shifts towards a
553 functional state, which reduces the energy cost of conformational changes required for
554 the cleavage of target strand and the release of the products.

555 Our findings reveal that unbound Mn^{2+} play an important role in the endonuclease
556 functions of pAgo proteins, and this mechanism is a general strategy employed by pAgo
557 proteins from mesophilic, thermophilic, and hyperthermophilic organisms to enhance
558 their catalytic functions. Unlike previous structural studies, which highlight the
559 importance of the bound Mn^{2+} in directly participating in guide binding and target
560 cleavage, our work discovers a role of unbound Mn^{2+} in an indirect way. We found that
561 unbound free Mn^{2+} plays a crucial part in promoting the structural flexibility of pAgo
562 proteins. This benefit extends not only to the binding of the protein to guide and target
563 DNA, but also to the cleavage and release processes.

564 More importantly, by harnessing the influence of protein flexibility induced by
565 unbound Mn^{2+} on the degree of mismatch between guide and target nucleic acids, we
566 can finely tune the precision of target recognition by pAgo proteins through the
567 modulation of Mn^{2+} concentration. This crucial characteristic expands the scope of

568 molecular diagnostic applications, further highlighting the significance of structural
569 flexibility in optimizing the performance of pAgo proteins.
570

571 **MATERIALS AND METHODS**

572 **Protein expression and purification**

573 A codon-optimized version of the *Pf*Ago, *Tt*Ago, *Fp*Ago, *Mf*Ago, *Bl*Ago, *Pb*Ago,
574 *Cb*Ago, *Cb*Ago*M*, and *Pli*Ago gene was synthesized by Sangon Biotech (Shanghai,
575 China), and was cloned into the pET28a plasmid to construct pEX-Ago with an N
576 terminal His-tag. The expression plasmid was transformed into *Escherichia coli*
577 BL21(DE3) cells. A 10 ml seed culture was grown at 37 ºC in LB medium with 50
578 μg/ml kanamycin and was subsequently transferred to 1 L of LB in a shaker flask
579 containing 50 μg/ml kanamycin. The cultures were incubated at 37 ºC until the OD_{600}
580 reached 0.6-0.8, and protein expression was then induced by the addition of isopropyl-
581 D-thiogalactopyranoside (IPTG) to a final concentration of 0.5 mM, followed by
582 incubation for 20-24 h at 18 ºC. Cells were harvested by centrifugation for 30 min at
583 6,000 rpm, and the cell pellets were collected for later purification. The cell pellets were
584 resuspended in lysis buffer (15 mM Tris-HCl, 500 mM NaCl, pH 7.4) and then
585 disrupted using a High-Pressure Homogenizer at 700-800 bar for 5 min (Gefran, Italy).
586 The lysates were centrifuged for 30 min at 12,000 rpm at 4 ºC, after which the
587 supernatants were subjected to Ni-NTA affinity purification with elution buffer (15 mM
588 Tris-HCl, 500 mM NaCl, 250 mM imidazole, pH 7.4). Further gel filtration purification
589 using a Superdex 200 (GE Tech, USA) was carried out with an elution buffer. The
590 fractions resulting from gel filtration were analyzed by SDS-PAGE, and fractions
591 containing the protein were flash frozen at -80 ºC in buffer (15 mM Tris–HCl pH 7.4,
592 200 mM NaCl, 10% glycerin).

593

594 **Differential scanning fluorimetry**

595 Each pAgo protein sample containing 1 μM of protein in a buffer containing 15 mM
596 Tris-HCl (pH = 7.4) and 200 mM NaCl was prepared in triplicate and added to PCR
597 tubes. To examine the effect of Mn^{2+} on pAgo proteins, pAgo proteins were incubated
598 in Tris-HCl buffer (pH = 7.4) with 5 mM Mn^{2+} or 5 mM EDTA for 20 min. SYPRO
599 Orange dye available as 5000× stock (Sigma-Aldrich) was added just before the
600 measurement of the pAgo proteins in an appropriate amount to achieve a final

601 concentration of the dye of 5×. The thermal denaturation of the pAgo proteins was
602 monitored by exciting the SYPRO Orange dye at 470 nm and monitoring its
603 fluorescence emission at 570 nm using Q-PCR (Analytikjena, Germany). The baseline
604 correction is used by the Opticon Monitor software available on the PCR instrument.
605
606 **Nano differential scanning calorimetry**
607 Nano differential scanning calorimetry (nanoDSC) measurements were performed by
608 using Nano DSC instruments (TA, USA). The concentration of pAgo proteins was 0.1
609 mg/mL in a buffer containing 15 mM Tris-HCl (pH 7.4) and 200 mM NaCl. To examine
610 the effect of Mn^{2+} on pAgo proteins, p*Ago* proteins were incubated in 15 mM Tris-HCl
611 buffer (pH = 7.4) with 5 mM Mn^{2+} or 5 mM EDTA for 20 min. All the experiments
612 were carried out at temperatures ranging from 10 to 110 ºC with a heating rate of 1
613 ºC/min and under a pressure of 3 atm. The melting curves of pAgo proteins were
614 subtracted from the buffer scans.
615
616 **Circular dichroism spectroscopy**
617 The CD measurements on the evolution of the secondary structure of pAgo proteins
618 were performed in a Jasco J-1500 spectropolarimeter with a 1 mm pathlength cell. The
619 signals in the far-UV CD region (222 nm) were monitored as a function of temperature
620 to determine the thermal unfolding of pAgo proteins. The concentrations of pAgo
621 proteins were 0.1 mg/mL in 1× PBS buffer (pH = 7.4) for the various measurements.
622 The pAgo proteins were heated in the range of 15 ºC to 100 ºC with a 1 ºC/min heating
623 rate and equilibrated for 3 min at each temperature, and the CD data were collected at
624 0.5 ºC intervals. For CD spectra, we used PBS buffer as the solvent instead of Tris-HCl
625 buffer because the Tris-HCl buffer has a strong CD background, which will
626 significantly affect the analysis of the CD signal of proteins (24).
627
628 **Small-angle X-ray scattering**
629 Small-angle X-ray scattering (SAXS) measurement was employed to monitor the
630 structural evolution of pAgo proteins incubated with and without Mn^{2+}. In-situ

synchrotron SAXS measurements were conducted at BL19U2 beamline in Shanghai Synchrotron Radiation Facility (SSRF). The X-ray wavelength was 0.103 nm. Protein samples were dissolved in a buffer containing 15 mM Tris-HCl (pH 7.4), 200 mM NaCl and 5 mM $MnCl_2$ or EDTA. The concentration of samples is 0.5 mg/ml. Protein solutions were loaded into the silica cell and then gently refreshed with a syringe pump to prevent X-ray damage. The measurements were carried out at 25 ^{o}C. In order to calculate the absolute intensity of protein, the empty cell and buffer were also measured at corresponding temperatures. Two-dimensional (2D) diffraction patterns were collected by the Pilatus 2 M detector with a resolution of 1043 × 981 pixels of 172 μm × 172 μm. Twenty sequential 2D images were collected with 0.5 s exposure time per frame. The 2D scattering patterns were then integrated into one-dimensional (1D) intensity curves by using Fit2D software from European Synchrotron Radiation Facility (ESRF). Frames with no radiation damage were used for further processing. The SAXS data were compared to the atomic model by using CRYSOL software (57). *ab initio* reconstruction of protein structure by a chain-like ensemble of dummy residues is generated by GASBOR (58). P1(no symmetry) and monodisperse data mode were used in generating the GASBOR model. At least 10 iterations of GASBOR programs were independently performed to validate the models. A presentative of the most typical model obtained was used in the figures. The one-dimensional data is processed by using *ScÅtter* and ATSAS software (59). The details of SAXS data collection and analysis are summarized in Table S3.

Molecular dynamics simulations

The initial structures of *Cb*Ago and *Tt*Ago for simulations were taken from PDB crystal structures 6QZK and 4N47, respectively. The initial structures of *Bl*Ago and *Fp*Ago for simulations were taken from AlphaFold2 (60). The initial structure of *Cb*Ago-gDNA-tDNA for simulations was taken from PDB crystal structures 6QZK. Protein and a large number of water molecules were filled in a cubic box (see Figure S5). For proteins and complexes incubated with the Mn^{2+} system, 6 Mn^{2+} were added into the simulation box to mimic the experimental concentration, and 32 chlorine counter ions were added

661 to keep the system neutral in charge. For proteins and complexes in an aqueous solution,
662 16 chlorine counter ions were added to keep the system neutral in charge. The
663 CHARMM36m force field (61) was used for proteins, complex, and Mn^{2+}, and the
664 CHARMM-modified TIP3P model was chosen for water. The simulations were carried
665 out at 298 K. After the 4000-step energy-minimization procedure, the systems were
666 heated and equilibrated for 100 ps in the NVT ensemble and 500 ps in the NPT ensemble.
667 The 100-ns production simulationswere carried out at 1 atm with the proper periodic
668 boundary condition, and the integration step was set to 2 fs. Fig. S3 shows the 100 ns
669 profile of potential energy as a function of MD trajectory time for *Cb*Ago incubated
670 with and without Mn^{2+}. It was clear that the equilibration procedure was sufficient for
671 minimizing the energy of protein structures. The covalent bonds with hydrogen atoms
672 were constrained by the LINCS algorithm (62). Lennard-Jones interactions were
673 truncated at 12 Å with a force-switching function from 10 to 12 Å. The electrostatic
674 interactions were calculated using the particle mesh Ewald method (63) with a cutoff
675 of 12 Å on an approximately 1 Å grid with a fourth-order spline. The temperature and
676 pressure of thesystem are controlled by the velocity rescaling thermostat (64) and the
677 Parrinello-Rahman algorithm (65), respectively. All MD simulations were performed
678 using GROMACS 2020.4 software packages. Representative simulation snapshots of
679 the systems are given in Figure S5.
680
681 **Single-strand DNA cleavage assay**
682 For standard activity assays, cleavage experiments were performed in a 5:1:1 molar
683 ratio (protein:guide:target). First, 5 μM pAgo protein was mixed with a synthetic 1 μM
684 gDNAguide in the reaction buffer (15 mM Tris-HCl (pH 7.4), 200 mM NaCl, different
685 concentrations of $MnCl_2$ or 5 mM EDTA). The solution was then pre-incubated at 37 °C
686 for 20 min. After pre-incubation, 1 μM tDNA, which was labeled with the fluorescent
687 group 6-FAM at the 5'-end and the quencher BHQ1 at the 3'-end, was added to the
688 mixture. The cleavage experiments were performed at 37 °C. All experiments were
689 performed in triplicate, and the fluorescence signals were traced by the quantitative
690 real-time PCR QuantStudio 5 (Thermo Fisher Scientific, USA) with λ_{ex} = 495 nm and

691 λ_{em} = 520 nm. The results were analyzed by QuantStudio™ Design & Analysis
692 Software v1.5.1. All the gDNA and tDNA used for cleavage are listed in Table S4.
693
694 **Fluorescence Polarization Assay**
695 To determine the apparent dissociation constant (K_d) for pAgo proteins binding to either
696 guide DNA or target DNA, a fluorescence polarization assay was conducted utilizing a
697 multifunctional enzyme-linked immunosorbent assay plate reader (Spark, Tecan). A
698 solution was prepared by combining 5 nM of 3'6-FAM labeled guide or target DNA
699 with pAgo proteins in a range of concentrations from 0 to 1500 nM in a reaction buffer
700 (15 mM Tris-HCl, pH 7.4, 200 mM NaCl, and varying concentrations of $MnCl_2$). This
701 mixture was incubated at 37°C for 20 minutes and then transferred to a light-protected
702 96-well ELISA plate. The degree of polarization was measured using the Spark Tecan
703 plate reader, with an excitation wavelength of 485 nm and an emission wavelength of
704 525 nm. The resulting data were processed via non-linear regression using the one-site
705 total binding model in GraphPad Software's Prism 8, to calculate the K_d value.
706
707 **Data availability**
708 All the data are presented in SI.
709
710 **Funding**
711 This work was supported by NSF China (11504231, 31630002, and 22063007) and the
712 Innovation Program of Shanghai Municipal Education Commission, National Key
713 Research & Development Program of China (2018YFA0900403), Shanghai Pilot
714 Program for Basic Research-Shanghai Jiao Tong University (21TQ1400204).
715
716 **Acknowledgments**
717 We would like to thank the Instrumental Analysis Center of Shanghai Jiao Tong
718 University for assistance with thermal performance tests via nanoDSC and CD. We
719 would like to thank Dr. Na Li from BL19U2 beamline of Shanghai Synchrotron
720 Radiation Facility (SSRF) for the help with synchrotron X-ray measurements on No.
721 h20pr0008.
722
723 **Additional information**
724 Correspondence and requests for materials should be addressed to
725 hongl3liang@sjtu.edu.cn, liuqian1018@sjtu.edu.cn.
726

Competing financial interests

The authors declare no competing financial interests.

Supplementary Information:

Figures S1-S23

Tables S1-S6

734 **References**

735 1. B. Koopal *et al.*, Short prokaryotic Argonaute systems trigger cell death upon detection of
736 invading DNA. *Cell* **185**, 1471-1486.e1419 (2022).
737 2. D. C. Swarts *et al.*, DNA-guided DNA interference by a prokaryotic Argonaute. *Nature* **507**, 258-
738 261 (2014).
739 3. D. C. Swarts *et al.*, The evolutionary journey of Argonaute proteins. *Nature Structural &*
740 *Molecular Biology* **21**, 743-753 (2014).
741 4. J. W. Hegge, D. C. Swarts, J. van der Oost, Prokaryotic Argonaute proteins: novel genome-
742 editing tools? *Nature Reviews Microbiology* **16**, 5-11 (2018).
743 5. J. Song *et al.*, Highly specific enrichment of rare nucleic acid fractions using Thermus
744 thermophilus argonaute with applications in cancer diagnostics. *Nucleic Acids Research* **48**,
745 e19-e19 (2019).
746 6. Q. Liu *et al.*, Argonaute integrated single-tube PCR system enables supersensitive detection of
747 rare mutations. *Nucleic Acids Research* **49**, e75-e75 (2021).
748 7. R. He *et al.*, Pyrococcus furiosus Argonaute-mediated nucleic acid detection. *Chemical*
749 *Communications* **55**, 13219-13222 (2019).
750 8. Y. Qin, Y. Li, Y. Hu, Emerging Argonaute-based nucleic acid biosensors. *Trends in Biotechnology*
751 **40**, 910-914 (2022).
752 9. X. Li *et al.*, Mesophilic Argonaute-based isothermal detection of SARS-CoV-2. *Frontiers in*
753 *Microbiology* **13** (2022).
754 10. R. Vaiskunaite, J. Vainauskas, J. J. L. Morris, V. Potapov, J. Bitinaite, Programmable cleavage of
755 linear double-stranded DNA by combined action of Argonaute CbAgo from Clostridium
756 butyricum and nuclease deficient RecBC helicase from E. coli. *Nucleic Acids Research* **50**, 4616-
757 4629 (2022).
758 11. G. Xun, S. T. Lane, V. A. Petrov, B. E. Pepa, H. Zhao, A rapid, accurate, scalable, and portable
759 testing system for COVID-19 diagnosis. *Nature Communications* **12**, 2905 (2021).
760 12. J. Song *et al.*, Highly specific enrichment of rare nucleic acid fractions using Thermus
761 thermophilus argonaute with applications in cancer diagnostics. *Nucleic Acids Research* **48**,
762 e19-e19 (2020).
763 13. F. Wang *et al.*, PfAgo-based detection of SARS-CoV-2. *Biosensors and Bioelectronics* **177**,
764 112932 (2021).
765 14. G. Xun *et al.*, Argonaute with stepwise endonuclease activity promotes specific and multiplex
766 nucleic acid detection. *Bioresources and Bioprocessing* **8**, 46 (2021).
767 15. M. Filius *et al.*, High-Speed Super-Resolution Imaging Using Protein-Assisted DNA-PAINT. *Nano*
768 *Letters* **20**, 2264-2270 (2020).
769 16. L. Chang *et al.*, AgoFISH: cost-effective in situ labelling of genomic loci based on DNA-guided
770 dTtAgo protein. *Nanoscale Horizons* **4**, 918-923 (2019).
771 17. A. Toudji-Zouaz, V. Bertrand, A. Barrière, Imaging of native transcription and transcriptional
772 dynamics in vivo using a tagged Argonaute protein. *Nucleic Acids Research* **49**, e86-e86 (2021).
773 18. S. Shin *et al.*, Quantification of purified endogenous miRNAs with high sensitivity and specificity.
774 *Nature Communications* **11**, 6033 (2020).
775 19. K. S. Makarova, Y. I. Wolf, J. van der Oost, E. V. Koonin, Prokaryotic homologs of Argonaute
776 proteins are predicted to function as key components of a novel system of defense against
777 mobile genetic elements. *Biology Direct* **4**, 29 (2009).

20. S. Willkomm, K. S. Makarova, D. Grohmann, DNA silencing by prokaryotic Argonaute proteins adds a new layer of defense against invading nucleic acids. *FEMS Microbiology Reviews* **42**, 376-387 (2018).
21. G. Sheng *et al.*, Structure-based cleavage mechanism of Thermus thermophilus Argonaute DNA guide strand-mediated DNA target cleavage. *Proc Natl Acad Sci U S A* **111**, 652-657 (2014).
22. L. Lisitskaya, A. A. Aravin, A. Kulbachinskiy, DNA interference and beyond: structure and functions of prokaryotic Argonaute proteins. *Nature Communications* **9**, 5165 (2018).
23. Y. Wang *et al.*, Nucleation, propagation and cleavage of target RNAs in Ago silencing complexes. *Nature* **461**, 754-761 (2009).
24. L. Zheng *et al.*, Loosely-packed dynamical structures with partially-melted surface being the key for thermophilic argonaute proteins achieving high DNA-cleavage activity. *Nucleic Acids Research* **50**, 7529-7544 (2022).
25. S. Willkomm *et al.*, Structural and mechanistic insights into an archaeal DNA-guided Argonaute protein. *Nature Microbiology* **2**, 17035 (2017).
26. S. Willkomm *et al.*, Single-molecule FRET uncovers hidden conformations and dynamics of human Argonaute 2. *Nature Communications* **13**, 3825 (2022).
27. Y. Wang, G. Sheng, S. Juranek, T. Tuschl, D. J. Patel, Structure of the guide-strand-containing argonaute silencing complex. *Nature* **456**, 209-213 (2008).
28. P. B. Kwak, Y. Tomari, The N domain of Argonaute drives duplex unwinding during RISC assembly. *Nature Structural & Molecular Biology* **19**, 145-151 (2012).
29. T. Miyoshi, K. Ito, R. Murakami, T. Uchiumi, Structural basis for the recognition of guide RNA and target DNA heteroduplex by Argonaute. *Nature Communications* **7**, 11846 (2016).
30. L. Lisitskaya *et al.*, Programmable RNA targeting by bacterial Argonaute nucleases with unconventional guide binding and cleavage specificity. *Nature Communications* **13**, 4624 (2022).
31. J. W. Hegge *et al.*, DNA-guided DNA cleavage at moderate temperatures by Clostridium butyricum Argonaute. *Nucleic Acids Research* **47**, 5809-5821 (2019).
32. J. S. Parker, E. A. Parizotto, M. Wang, S. M. Roe, D. Barford, Enhancement of the Seed-Target Recognition Step in RNA Silencing by a PIWI/MID Domain Protein. *Molecular Cell* **33**, 204-214 (2009).
33. A. Zander *et al.*, Guide-independent DNA cleavage by archaeal Argonaute from Methanocaldococcus jannaschii. *Nature Microbiology* **2**, 17034 (2017).
34. E. Kaya *et al.*, A bacterial Argonaute with noncanonical guide RNA specificity. *Proceedings of the National Academy of Sciences* **113**, 4057-4062 (2016).
35. H. Dong *et al.*, Characterization of Argonaute nucleases from mesophilic bacteria Paenibacillus borealis and Brevibacillus laterosporus. *Bioresources and Bioprocessing* **8**, 133 (2021).
36. D. C. Swarts *et al.*, Argonaute of the archaeon Pyrococcus furiosus is a DNA-guided nuclease that targets cognate DNA. *Nucleic Acids Research* **43**, 5120-5129 (2015).
37. Y. Chong, Q. Liu, F. Huang, D. Song, Y. Feng, Characterization of a recombinant thermotolerant argonaute protein as an endonuclease by broad guide utilization. *Bioresources and Bioprocessing* **6**, 21 (2019).
38. X. Guo *et al.*, A Hyperthermophilic Argonaute From Ferroglobus placidus With Specificity on Guide Binding Pattern. *Frontiers in Microbiology* **12** (2021).
39. R. W. Woody, "[4] Circular dichroism" in Methods in Enzymology. (Academic Press, 1995), vol.

822 246, pp. 34-71.
823 40. F. H. Niesen, H. Berglund, M. Vedadi, The use of differential scanning fluorimetry to detect
824 ligand interactions that promote protein stability. *Nature Protocols* **2**, 2212-2221 (2007).
825 41. G. M. D. Ferreira *et al.*, Lactoferrin denaturation induced by anionic surfactants: The role of the
826 ferric ion in the protein stabilization. *International Journal of Biological Macromolecules* **117**,
827 1039-1049 (2018).
828 42. R. P. Rambo, J. A. Tainer, Characterizing flexible and intrinsically unstructured biological
829 macromolecules by SAS using the Porod-Debye law. *Biopolymers* **95**, 559-571 (2011).
830 43. R. P. Rambo, J. A. Tainer, Super-Resolution in Solution X-Ray Scattering and Its Applications to
831 Structural Systems Biology. *Annual Review of Biophysics* **42**, 415-441 (2013).
832 44. K. Sharma, I. L. Antunes, V. Rajulapati, A. Goyal, Low-resolution SAXS and comparative
833 modeling based structure analysis of endo-β-1,4-xylanase a family 10 glycoside hydrolase from
834 Pseudopedobacter saltans comb. nov. *International Journal of Biological Macromolecules* **112**,
835 1104-1114 (2018).
836 45. C. Putnam, Guinier peak analysis for visual and automated inspection of small-angle X-ray
837 scattering data. *Journal of Applied Crystallography* **49**, 1412-1419 (2016).
838 46. William E. Salomon, Samson M. Jolly, Melissa J. Moore, Phillip D. Zamore, V. Serebrov, Single-
839 Molecule Imaging Reveals that Argonaute Reshapes the Binding Properties of Its Nucleic Acid
840 Guides. *Cell* **162**, 84-95 (2015).
841 47. D. C. Swarts *et al.*, Autonomous Generation and Loading of DNA Guides by Bacterial Argonaute.
842 *Molecular Cell* **65**, 985-998.e986 (2017).
843 48. K. W. Doxzen, J. A. Doudna, DNA recognition by an RNA-guided bacterial Argonaute. *PLOS ONE*
844 **12**, e0177097 (2017).
845 49. C. Wang, D. A. Greene, L. Xiao, R. Qi, R. Luo, Recent Developments and Applications of the
846 MMPBSA Method. *Frontiers in Molecular Biosciences* **4** (2018).
847 50. J. Li, X. Zhang, L. Hong, Y. Liu, Entropy Driving the Mg2+-Induced Folding of TPP Riboswitch RNA.
848 *The Journal of Physical Chemistry B* **126**, 9457-9464 (2022).
849 51. J. L. Fiore, E. D. Holmstrom, D. J. Nesbitt, Entropic origin of Mg2+-facilitated RNA folding.
850 *Proceedings of the National Academy of Sciences* **109**, 2902-2907 (2012).
851 52. H. Son *et al.*, Mg2+-dependent conformational rearrangements of CRISPR-Cas12a R-loop
852 complex are mandatory for complete double-stranded DNA cleavage. *Proceedings of the*
853 *National Academy of Sciences* **118**, e2113747118 (2021).
854 53. C. Andreini, I. Bertini, G. Cavallaro, G. L. Holliday, J. M. Thornton, Metal ions in biological
855 catalysis: from enzyme databases to general principles. *JBIC Journal of Biological Inorganic*
856 *Chemistry* **13**, 1205-1218 (2008).
857 54. C. Hureau, P. Faller, Aβ-mediated ROS production by Cu ions: Structural insights, mechanisms
858 and relevance to Alzheimer's disease. *Biochimie* **91**, 1212-1217 (2009).
859 55. F. H. Yu, W. A. Catterall, The VGL-Chanome: A Protein Superfamily Specialized for Electrical
860 Signaling and Ionic Homeostasis. *Science's STKE* **2004**, re15 (2004).
861 56. Y. Nevo, N. Nelson, The NRAMP family of metal-ion transporters. *Biochimica et Biophysica Acta*
862 *(BBA) - Molecular Cell Research* **1763**, 609-620 (2006).
863 57. D. Svergun, C. Barberato, M. H. J. Koch, CRYSOL - a Program to Evaluate X-ray Solution
864 Scattering of Biological Macromolecules from Atomic Coordinates. *Journal of Applied*
865 *Crystallography* **28**, 768-773 (1995).

58. D. I. Svergun, M. V. Petoukhov, M. H. J. Koch, Determination of Domain Structure of Proteins from X-Ray Solution Scattering. *Biophysical Journal* **80**, 2946-2953 (2001).
59. K. Manalastas-Cantos *et al.*, ATSAS 3.0: expanded functionality and new tools for small-angle scattering data analysis. *Journal of Applied Crystallography* **54**, 343-355 (2021).
60. J. Jumper *et al.*, Highly accurate protein structure prediction with AlphaFold. *Nature* **596**, 583-589 (2021).
61. J. Huang *et al.*, CHARMM36m: an improved force field for folded and intrinsically disordered proteins. *Nature Methods* **14**, 71-73 (2017).
62. B. Hess, C. Kutzner, D. van der Spoel, E. Lindahl, GROMACS 4: Algorithms for Highly Efficient, Load-Balanced, and Scalable Molecular Simulation. *Journal of Chemical Theory and Computation* **4**, 435-447 (2008).
63. U. Essmann *et al.*, A smooth particle mesh Ewald method. *The Journal of Chemical Physics* **103**, 8577-8593 (1995).
64. G. Bussi, D. Donadio, M. Parrinello, Canonical sampling through velocity rescaling. *The Journal of Chemical Physics* **126**, 014101 (2007).
65. M. Parrinello, A. Rahman, Polymorphic transitions in single crystals: A new molecular dynamics method. *Journal of Applied Physics* **52**, 7182-7190 (1981).